Nucleation-Controlled Distributed Plasticity in Penta-twinned Silver Nanowires

*Tobin Filleter, Seunghwa Ryu, Keonwook Kang, Jie Yin, Rodrigo A. Bernal, Kwonnam Sohn, Shuyou Li, Jiaxing Huang, Wei Cai, and Horacio D. Espinosa**

***A** unique size-dependent strain hardening mechanism, that achieves both high strength and ductility, is demonstrated for penta-twinned Ag nanowires (NWs) through a combined experimental-computational approach. Thin Ag NWs are found to deform via the surface nucleation of stacking fault decahedrons (SFDs) in multiple plastic zones distributed along the NW. Twin boundaries lead to the formation of SFD chains that locally harden the NW and promote subsequent nucleation of SFDs at other locations. Due to surface undulations, chain reactions of SFD arrays are activated at stress concentrations and terminated as local stress decreases, revealing insensitivity to defects imparted by the twin structures. Thick NWs exhibit lower flow stress and number of distributed plastic zones due to the onset of necking accompanied by more complex dislocation structures.*

1. Introduction

Plasticity in thin films and micro-pillars shows increasing flow stress as the characteristic dimension decreases from 10 micrometers down to 100 nm.[1] This behavior has been attributed to dislocation motion/multiplication mechanisms, primarily through the so-called "source shut-down" mechanism.[2–4] Studies of metallic nano-pillars, with characteristic dimensions of a few hundred nms, have demonstrated size-effects in flow stress and strain hardening attributed to "dislocation starvation" after which dislocation nucleation is required to accommodate further plasticity.[5–7] By contrast, face-centered cubic (FCC) metal nanowires (NWs), whose diameters are below 100 nm, are dislocation free prior to deformation. Under this condition, dislocation nucleation becomes the controlling plastic deformation mechanism.[8] Although there have been many molecular dynamics simulations on the plastic deformation of metal nanowires,[9,10] most of the predictions have not been tested experimentally due to the difficulty of conducting in-situ transmission electron microscopy (TEM) tensile measurements in which the plastic deformation mechanisms can be directly identified. Recently plastic deformation in sub-10-nm crystals has been shown to be controlled by the nucleation of dislocations at free surfaces.[11] However, in-situ TEM uniaxial stress-strain responses of *synthesized,* long uniform-cross-section metal nanowires have not been reported.

The plastic deformation of single crystal metal nanowires has been predicted by molecular dynamics simulations to be the result of slip (by perfect or partial dislocations) or twinning, depending on the wire orientation and tension/compression mode.[12] Experimental tensile measurements on single crystal metal (micro and nano) whiskers[13,14] show high strength but little ductility, due to highly localized plastic deformation once the first dislocation is nucleated. Single crystal Au NWs have recently been reported to exhibit high ductility accompanied by low strength and a significant stress reduction after yield

Dr. T. Filleter,[+] R. A. Bernal, Dr. S. Li, Prof. H. D. Espinosa
Department of Mechanical Engineering
Northwestern University, Evanston IL 60208
E-mail: espinosa@northwestern.edu
Dr. S. Ryu, Dr. K. Kang,[++] J. Yin, Prof. W. Cai
Department of Mechanical Engineering
Stanford University, Stanford CA 94305
K. Sohn, Prof. J. Huang
Department of Materials Science and Engineering
Northwestern University
Evanston IL 60208
[+] Present Address: Department of Mechanical and Industrial Engineering, University of Toronto, Toronto ON, Canada M5S 3G8
[++] Present Address: Los Alamos National Laboratory, Los Alamos NM 875448

DOI: 10.1002/smll.201200522

NANO MICRO small

induced by coherent twin propagation, which reorients the crystal.[15] Such lack of ductility and strain hardening undermines the mechanical robustness of metallic nanowires. It has been argued that metallic nanowires that incorporate twin boundaries, at regular intervals, may impede dislocation propagation and increase nanowire robustness.[9,16,17] Such an approach of strengthening via coherent nanoscale internal boundaries has been recently advanced as an attractive alternative to more classical methods, such as precipitate and grain boundary strengthening, due to its potential of preserving ductility along with high strength and work hardening.[18] Initial experimental demonstration of the benefits of incorporating nanotwins in metals have begun to emerge including materials such as nano-pillars of Cu,[19] foils of ultrafine crystalline Cu,[20,21] thin Pd[22] and Ag films.[23] Molecular dynamics simulations have also emerged to elucidate these benefits, for example large-scale simulations performed by Li et al which have reported a dislocation-nucleation-controlled mechanism in nano-twinned metals.[24] Atomic force microscopy (AFM) experiments of penta-twinned NWs have reported super elastic behavior with high yield strengths which are attributed to the role of twin boundary confinement.[16,25] However, the indirect nature and limitations in the spatial resolution of the AFM based experimental methods have prevented further insights into the identification of deformation mechanisms.

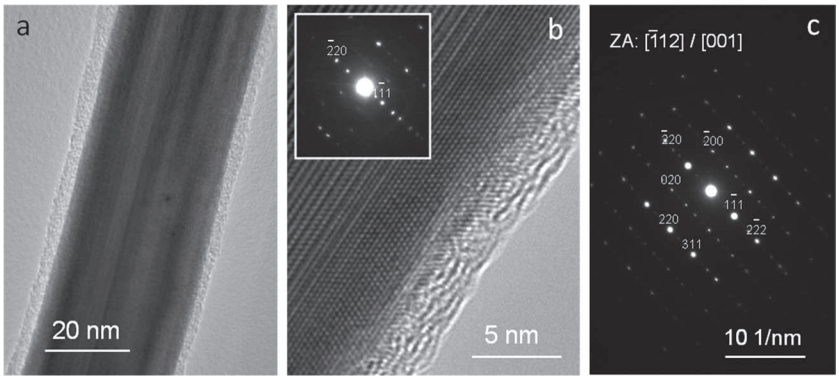

Figure 1. Penta-twinned Ag NWs. (a) Bright field TEM image of penta-twinned Ag NW. (b) HRTEM image of the edge of the same Ag NW shown in (a), the inset shows the SAED pattern of the NW revealing {111} fringes ($d_{\bar{2}20} = 0.144$, $d_{1\bar{1}1} = 0.238$). Note the NW is not perfectly aligned with low index zone axes. The fringe pattern in the center of the NW is due to double diffraction arising from the superposition of twin domains aligned along different zones. (c) Indexed SAED pattern of another penta-twinned Ag NW recorded with low index zone axes of [–1 1 2] and [0 0 1] with respect to two of the penta-twinned domains in the NW. The superposition of the two reciprocal lattices and the {111} fringes in the SAED is characteristic of the penta-twinned NW structure. Measured interplanar spacings: $d_{1\bar{1}1} = 0.240$, $d_{\bar{2}\bar{2}2} = 0.120$, $d_{311} = 0.124$, $d_{220} = 0.146$, $d_{020} = 0.2095$, $d_{\bar{2}20} = 0.148$, $d_{\bar{2}00} = 0.209$.

Using a combined approach of in-situ TEM micro-electro-mechanical systems (MEMS)-based tensile testing and atomistic simulations, we show that the coherent twin boundaries, present in penta-twined Ag NWs which contain five single crystal domains that extend the length of the [110] growth axis and intersect at {111} twin boundaries, result in a unique size-dependent strain hardening mechanism that can achieve both high strength and ductility. One-to-one comparison between stress-strain curves and microstructure evolution revealed through in-situ TEM tests shows that the NWs deform by nucleation of multiple local plastic regions distributed along the NW axis, in which each new nucleation event requires a stress increase, exhibiting strain hardening behavior. Interestingly, the number of active plastic deformation sites prior to failure increases with decreasing diameter, which means that strain hardening is more pronounced for thinner NWs. Atomistic simulations have identified that plasticity in the NWs proceed by the formation of a series of stacking fault decahedron (SFD) along the NW axis. The nucleation of the first partial dislocation leads to a SFD that facilitates the formation of neighboring SFDs, until the chain reaction stops due to surface irregularities (such as surface dimples), locally hardening the NW in the vicinity of the SFD array. Consequently, higher nucleation stress is required to initiate SFD chains elsewhere. As the NW diameter increases, more complex SFD and dislocation structures tend to form, leading to earlier necking. The ability to directly compare atomistic experiments and simulations is here epitomized by providing a significant step toward a fundamental understanding of plastic deformation in metallic nanomaterials.

2. Results and Discussion

Long (~5–10 μm) Ag penta-twinned NWs (see **Figure 1**) were synthesized by a modified polyol route[26,27] with diameters ranging from 40 to 120 nm (See Experimental Section for details). The unstrained crystalline structure of the tested NWs consists of five single crystal domains that intersect at {111} twin boundaries and run the length of the NW axis parallel to the [110] growth direction, as revealed through selected area electron diffraction (SAED) (see Figure 1c).[28] The surfaces of the synthesized NWs are of high quality (see Figure 1a,b) and the NWs have few defects (other than the five twin boundaries), making them good candidates to compare with atomistic simulations.

Tensile tests were conducted in-situ a JEOL 2100F field emission TEM operated at 200 keV using MEMS devices, in which both stress and strain are measured during the deformation, while the NW atomic structure is directly observed in the TEM.[29,30] Prior to tensile testing individual penta-twinned Ag NWs were identified in-situ a FEI Nova Nano 600 SEM and manipulated using a nanomanipulator (Klocke Nanotechnik) onto the MEMS device. Bonding between the Ag NWs and the two grip platforms of the testing device was achieved using e-beam induced deposition of Pt.[31] Tensile tests were conducted by applying a series of controlled displacements to a thermal actuator and the resulting force acting on the Ag NW at each step was determined from the deflection of the load sensor as described in detail previously.[30] Experimental stress-strain curves were calculated considering the engineering stress (using the initial cross-sectional area at zero stress for all stress measurements) of the Ag NWs as well as the measured strain at each step determined directly from TEM images.

Although perfect alignment of the NW axis with the tensile axis of grip platforms was not possible, only NWs with a misalignment angle of below 25° as well as exhibiting ultimate failure in the gauge region and not near the edges of the grip platforms are reported here. Potential sources of error in stress measurement are discussed in detail in the Experimental Section and Section S1 of the Supplementary Information. These include possible systematic errors in the crossectional area of the NWs as well as the presence of a coating layer composed of both polyvinylpyrrolidone (PVP) (remaining from the synthesis of the NWs) (see Figure 1a,b) and amorphous carbon deposited during SEM and TEM imaging. An analysis of the measured elastic modulus as a function of the relative thickness of this coating layer for multiple experiments revealed that this coating layer may contribute up to ~11% error in the stress measurements (See SI Section S1).

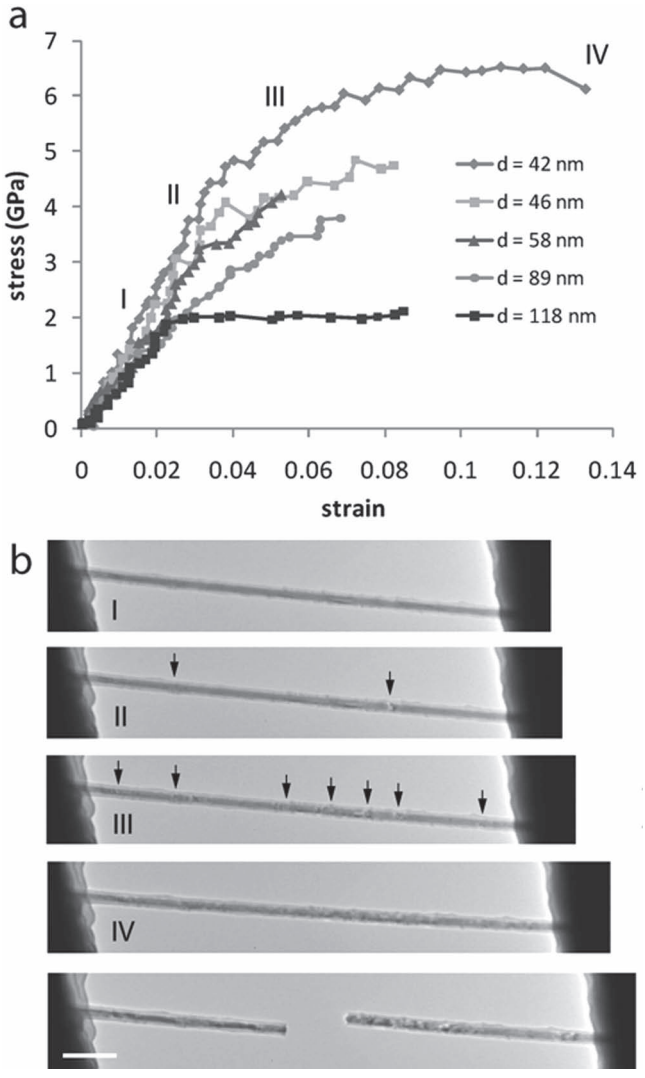

Figure 2. Experimental stress-strain response of penta-twinned Ag NWs. (a) Experimental stress-strain curves of Ag NWs of varying diameter. (b) Sequential bright field TEM images recorded during the tensile testing of a 42 nm diameter Ag NW. The arrows indicate localized regions of plastic deformation nucleated during the tensile test. The roman numerals indicate the point on the stress-strain curve in (a) at which each image was recorded. The bottom image was recorded after the NW fractured. The length of the scale bar is 250 nm.

Figure 2(a) shows the stress-strain responses of Ag NWs with varying diameter. Sequential TEM images recorded during a tensile test are shown in **Figure 2**(b) for the thinnest (42 nm diameter) Ag NW. At low strain the NWs are found to deform elastically with elastic modulus increasing with decreasing diameter (See Table S1 and Fig. S1b in Supplementary Information). The elastic modulus was computed from the slope of the stress-strain curves for the initial loading regime of below 2% strain. Smaller diameter NWs were found to exhibit moduli of up to 1.5 times the bulk value, which is consistent with previous experimental studies of Ag and Au NWs.[16,32,33] A summary of these previous experimental results can be found in Ref. [34] The initial yield strain, corresponding to the first plateau in the stress-strain curve, shows weak dependence on the NW diameter as one would expect from the nucleation theory[35] (see **Figure 3**(a)), which suggests that the onset of deformation is initiated by dislocation nucleation. However, the deformation behavior of the NWs after the initial yielding is significantly affected by the NW

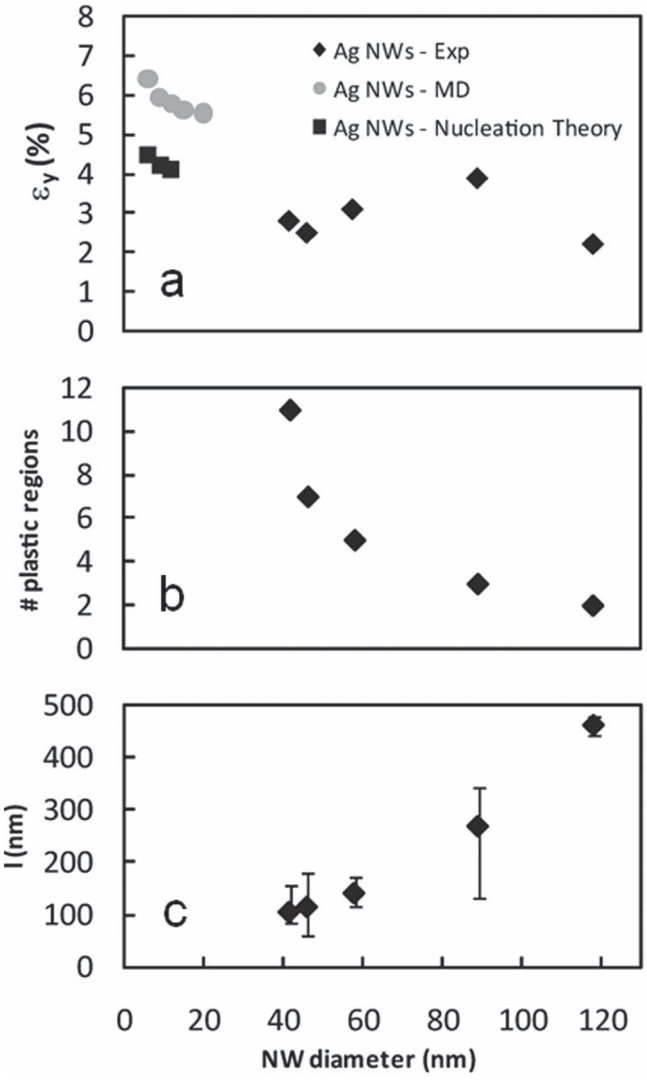

Figure 3. Comparison of (a) yield strain, (b) number of plastic regions, and (c) average length of plastic region, l, as a function of nanowire diameter.

small NANO MICRO

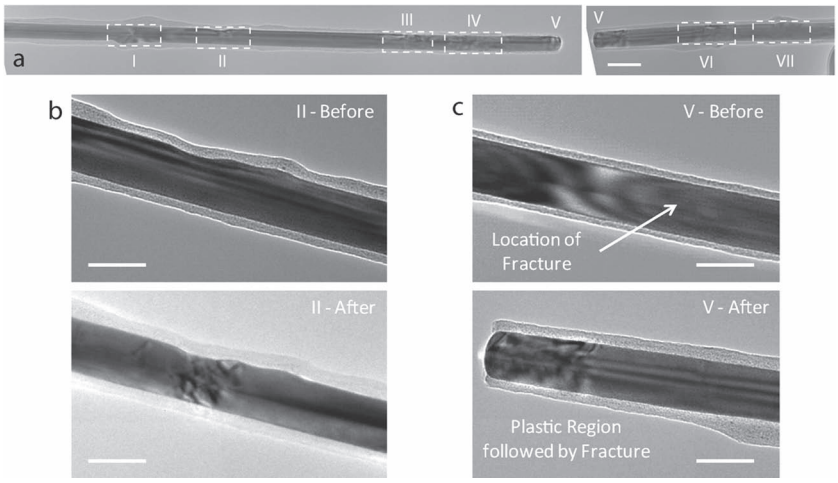

Figure 4. Discrete plastic zones distributed along Ag NWs. (a) TEM image of 46 nanometer diameter Ag nanowire after tensile testing exhibiting multiple plastically deformed regions. Scale bar: 100 nm. Images before and after deformation of (b) plastic region II, showing a strong surface imperfection in the shape of a dimple and (c) plastic region V, where fracture occurred. Scale bars: 50 nm.

diameter. Thinner NWs show a more pronounced strain hardening effect. The thickest tested NW (118 nm diameter), however, quickly develops necking with no strain hardening, which is similar to the behavior of single crystalline NWs.[13,14]

TEM images have revealed that dislocations are nucleated and propagated in discrete localized regions along the NWs. **Figure 4** (a) shows the location of seven plastically deformed zones, including the zone in which ultimate fracture occurs for an Ag NW with diameter of 46 nm. Through a comparison of TEM images recorded during tensile tests and the stress-strain responses we have found that plastic zones occur sequentially during the tensile tests (see Movie 1 for the 42 nm diameter NW) and correspond to the plateaus at different stress levels in the stress-strain curves. Before and after images of two representative local plastic zones are shown in Figure 4(b,c). The deformation mechanism and dislocation structure within the local plastic region are analyzed by atomistic simulations and will be discussed shortly.

Interestingly, the number of local plastic zones that develop during tensile testing is found to increase with decreasing NW diameter as shown in Figure 3(b). In the thickest tested nanowire, only two plastic zones developed during tensile deformation resulting in a stress-strain response exhibiting a strain hardening rate of nearly zero (~0.3 GPa) and an ultimate strength of only ~2 GPa, where the average strain hardening rate was calculated considering a Schmid factor of 0.47 and the slope of the stress-strain curve between the yield point and up to 7% strain. TEM imaging during the test (see Movie 2) demonstrated that after the initial yield the plastic zones grew in lateral extent along the NW and dislocations were nucleated and propagated only at these localized plastic zones. This was accompanied by significant necking (see Figure S2 of Supplementary Information), i.e., significant local reduction in the NW diameter in the plastically deformed regions (from 118.4 ± 0.3 nm to 110.0 ± 0.2 nm). In contrast the smallest diameter NW developed 11 localized plastic zones which nucleated at staggered intervals in the plastic deformation regime (see Movie 1 and Figure 2b). In this case the diameter of the NW in the plastically deformed regions was only slightly reduced (from 41.7 ± 0.2 nm to 40.6 ± 0.2 nm). Consequently, this small diameter NW exhibited an unprecedented combination of high strength, ductility, and strain hardening with a strain-to-failure of ~14% and strain hardening rate of 11.7 ± 0.4 GPa.

The extent of deformation during each plateau in the stress-strain curves promotes plastic strains of ~0.3–0.5% (or NW extensions of 8–12 nm) in which complex dislocation structures were formed as plastic zones. Also, the average axial extent (l) of each plastic zone was found to be proportional to the NW diameter as presented in Figure 3(c). From TEM imaging alone, it is not possible to determine exactly the dislocation structure and mechanism responsible for the formation of the plastic zones observed.

To reveal the atomistic detail of the deformation mechanism, we have performed MD simulations of penta-twinned Ag NWs under uniaxial tension at the strain rate of 10^7 s^{-1} at 300 K. The investigated NW diameters range from 6 nm to 20 nm. The interatomic interaction is described by the embedded atom method (EAM) potential.[36–38] In particular three EAM interatomic potential models[36–38] for silver were used for the MD simulations. The initial atomic structure is first relaxed to a local energy minimum using the conjugate gradient algorithm. The diameter of the penta-twinned NW, D, is defined for the circumscribed circle of the pentagonal cross section. The aspect ratio D/L of prepared NWs was 1:2.9. The periodic boundary condition (PBC) is applied along the NW axis. MD simulations were performed using the MD++[39] and LAMMPS[40] with time step of 0.2 fs. Before loading the NWs in tension, they were equilibrated for 50 ps in the NPT ensemble using the Langevin thermostat at 300 K and zero stress. The stress inside of the NWs is calculated using the Virial formula.[41,42] After equilibration, the tensile simulations were performed using the NVT ensemble using the Nose-Hoover thermostat, in which the NWs are elongated by 0.01% of the initial length at every 10 ps until the strain reaches 10%, corresponding to a strain rate of 10^7 s^{-1}. **Figure 5** presents typical stress-strain curves from the simulations. We do not observe a size dependent Young's modulus, as measured in the experiments. This discrepancy between simulation and experiments has been well recognized in the literature[34,43] and remains to be understood. Nonetheless, our simulations based on several EAM potential models all support our main conclusions regarding the plastic deformation mechanism of penta-twinned Ag NWs, which is controlled by dislocation nucleation and strongly influenced by the presence of twin boundaries.

In all MD simulations starting from a pristine penta-twinned NW containing no other defects than the five twin boundaries, plastic deformation was always found to begin by the nucleation of a partial dislocation from the NW surface.

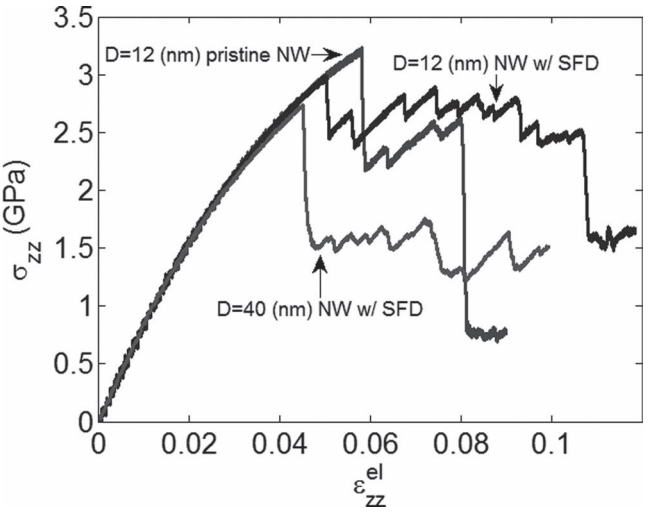

Figure 5. Stress-strain curves predicted by MD simulations of penta-twinned Ag NWs with diameter *D* under unaxial tension at the strain rate of 10^7 s^{-1} at 300 K. The data for both pristine NWs and NWs which contains one stacking fault decahedron (SFD) are shown.

As shown in **Figure 6**(a), the Shockley partial dislocation with Burgers vector pointing to the center axis of the NW nucleates on the surface area between two twin boundaries. This contradicts an earlier prediction that dislocations nucleate at the twin boundary of penta-twinned NWs.[9] This difference is likely caused by the smaller NW diameter investigated[9] (2.56 nm) where the cross section of the grain is smaller than the critical dislocation loop. Other previous MD simulations[24] have also shown that dislocations can nucleate at twin boundaries. Here, we find that in penta-twinned NWs, the surface is even more efficient than the twin boundary at nucleating dislocations. After this partial dislocation has swept the entire cross section of this grain, leaving a triangular shaped stacking fault area, it triggers dislocation activity on {111} slip planes in neighboring grains, leading to a five-sided hat-shaped stacking fault area. All dislocations in these five grains are partial dislocations with Burgers vector pointing to the center of the NW. Hence, there are residual edge dislocations at the twin boundaries, whose Burgers vector is the Burgers vector difference between dislocations on neighboring grains. At the same time, dislocations are also nucleated on the other set of {111} slip planes that are mirror reflections of the five-sided hat structure. Therefore, the first dislocation nucleation event quickly leads to the formation of a ten-sided stacking fault area, which we will call stacking fault decahedron (SFD), as shown in Figure 6(b) (For further details see Section S4 of the Supplementary Information). Subsequent microstructure evolution in the MD simulations can be characterized as the formation of more SFDs along the NW, as shown in Figure 6(c). The HRTEM image in Figure 6(d) presents the signature of SFD chains observed experimentally within the plastically deformed zones of the NWs.

Because of the differences in predicted and measured Young's modulus, as well as the possible systematic errors previously discussed in measuring the experimental stress, we focus our attention on yield strain (i.e., the elastic strain at the yield point) instead of yield stress. The MD predictions of yield strain are plotted in Figure 3(a). However, they should not be directly compared with experiments, because the MD strain rate is more than 10 orders of magnitude higher than the experimental strain rate (~5×10^{-4} s^{-1}). To extrapolate the yield strain to the experimental strain rate, we compute the energy barrier of the first dislocation nucleation event, using a modified version of the string method.[44] The energy barrier function E_b allows us to extrapolate the yield strain to the experimental strain rate[35] (See Experimental Section). As shown in **Figure 7** , an energy barrier of 1 eV predicts a yield strain of ~4% (see Figure 3(a)), which is in good agreement with the experimental measurements. The qualitative agreement between theoretical predictions and experimental measurements on the yield strain further support that the onset of yield is controlled by dislocation nucleation.

In order to understand why SFDs form in a regular array, we compute the energy barrier of partial dislocation nucleation on the NW surface at various distances *d* away from an existing SFD. We find that this energy barrier is at a minimum at the optimal value of d_{min} ~ 0.29 D, where D is the NW diameter. The linear scaling between d_{min} and D suggests that this effect is caused by the stress field of the residual dislocations at the twin boundaries of the first SFD. The energy barrier of the dislocation nucleation event that triggers the second SFD formation is significantly lower than that for the first SFD, as shown in Figure 7. This explains why the first SFD "catalyzes" the formation of the second SFD and why subsequent SFDs form as a regular array. The plastic strain produced by the formation of one SFD is approximately $\varepsilon_{SFD} = \delta_{SFD}/L$, where $\delta_{SFD} = 0.19$ nm and L is the total length of the NW. δ_{SFD} is twice the

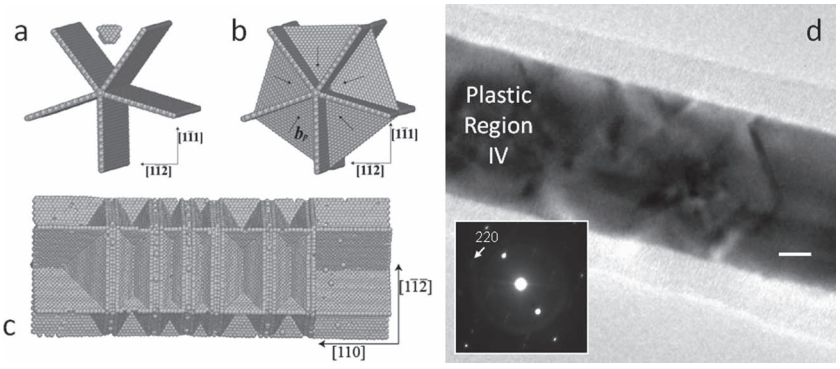

Figure 6. Surface nucleation of stacking fault decahedra (SFD) formation in thin Ag NWs. (a) Simulation snapshot of the first partial dislocation nucleation from a penta-twinned Ag NW with D = 12 nm. Only atoms with central symmetry parameter above 4.0 Å^2 and below 20 Å^2 are plotted, showing the five twin boundaries and dislocation nucleus. (b) Simulation snapshot showing the front side of the stacking fault decahedron (SFD) formed following the first dislocation nucleation event in (a). (c) A sequence of SFDs formed along the NW axis following the first SFD in (b). (d) TEM image of zone IV from Figure 4(a). The inset shows a SAED pattern recorded from the same NW region indicating the [110] growth direction (d_{220} = 0.148). Scale bar: 10 nm.

NANO MICRO small

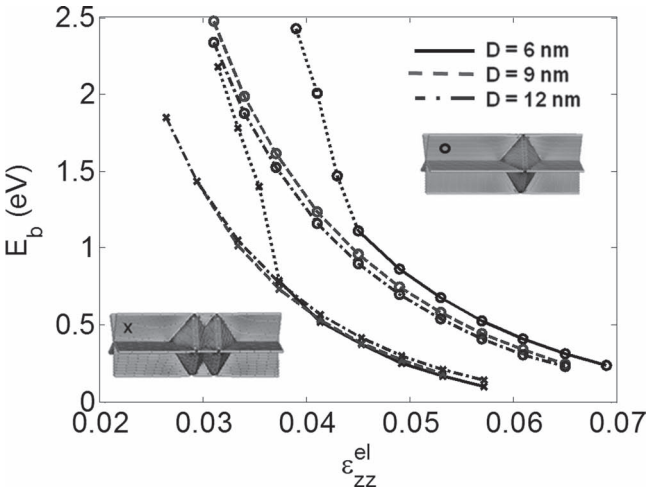

Figure 7. Energy barrier calculations of dislocation nucleation induced SFD formation. Energy barrier as a function of elastic strain for the dislocation nucleation event that leads to the formation of the first (circles) and second (crosses) SFD. D = NW diameter. For D = 6 nm NW at low strain (indicated by dotted lines), the critical dislocation nucleus is larger than the entire {111} slip plane of one grain, leading to a sharp rise of energy barrier (See SI S6).

projected length of the Shockley partial Burgers vector (see Figure 6) along the NW axis. Because L is several microns in the experiments, one ε_{SFD} is below the experimental resolution. Hence we propose that the strain bursts observed in the experiments are caused by the formation of linear chains of SFDs, as revealed by the simulations and observed experimentally (Figure 6).

MD simulations of pristine NWs always show a large stress drop immediately after yield. This is not observed in the experiments and is likely caused by the very high strain rate in the MD simulation. To nucleate the first dislocation within a few nanoseconds, the stress is much higher than necessary for maintaining subsequent plastic deformation. To avoid this overshooting of stress and make the simulation more representative of the experimental condition, we performed MD simulations of NWs already containing an SFD. In our simulations of NW with D = 12 nm containing one initial SFD, subsequently SFDs form and occupy almost the entire NW length before necking occurs. For real NWs, we do not expect dislocation activity to immediately propagate through the entire NW length once the first dislocation nucleates (nor do we observe that experimentally). Applying the understanding gained from the simulation to the experimental situation thus requires the acknowledgement that real NWs have surface undulations that create local stress concentrations. The location with the highest local stress field will be the place of the first dislocation nucleation, after which we expect the first SFD to form and to "catalyze" the formation of more SFDs in the neighborhood. As the SFD region expands away from the maximum stress location, new dislocations will have to be nucleated at surface locations with lower and lower stress. At some point, it is energetically more favorable to nucleate a leading partial dislocation at another stress concentrator, "catalyzing" the formation of another sequence of SFDs. This mechanism of distributing plasticity to multiple regions across the NW length is observed experimentally. In Figure 4 it can be seen that defects are initially formed in the region of a NW surface dimple (at which point the NW diameter is smaller) (Figure 4(b)) as well as subsequently at additional local slip regions (Figure 4(c)) at other points along the NW. Figure 4 also shows that the NW was locally hardened near the dimple and the SFD chain formation was arrested at the extremities of the dimple where the NW diameter was larger. Ultimate fracture of the NW occurred far from this point, demonstrating a unique insensitivity to surface irregularities facilitated by the presence of the twin boundaries in the thin NWs.

Experimentally, we observe that the number of local slip regions decreases with increasing NW diameter, with the largest diameter NW necking at one of the two local plastic zones. We also observe a size-dependence in the MD simulations of NWs containing one initial SFD. For the NW with D = 20 nm, the simulations show that new SFDs still form next to the existing SFDs, but necking also occurs almost simultaneously (See Figure S2a of the SI). Correspondingly, the stress also drops significantly. This behavior is quite different from the NW with D = 12 nm, where the stress remains close to the initial yield stress for a significant amount of plastic strain. Therefore, the simulations predict a transition of yield behavior as the NW diameter increases from 12 nm to 20 nm. This is in qualitative agreement with the transition observed in the experiments, except that in the experiments the transition occurs as D increases from ~40 nm to 100 nm. We believe that the difference in the transition diameter is due to the fact that the strain rate in MD simulations is 10 orders of magnitude higher than that in experiments. With increasing strain rate, dislocation nucleation processes that do not have the lowest energy barrier become increasingly competitive. This will lead to a more disorganized microstructure that will create dislocation sources and local necking, as observed in the MD simulations.

3. Conclusion

In summary, we have discovered size-dependent plasticity of Ag penta-twinned NWs through in-situ TEM experiments and elucidated the deformation mechanism by molecular dynamics simulations and energy barrier calculations. Unique strain hardening and multiple plastic zone formation in thin NWs (D < 100 nm) is explained by dislocation nucleation from a local stress concentrator, which leads to the formation of a linear chain of SFDs. By confining dislocation activity to SFD chain propagation, the internal twin boundaries cause local hardening of thin NWs, resulting in defect insensitive structures with significantly enhanced flow stress, ductility and strength. As NW diameter becomes larger, the number of local plastic zones decreases due to the earlier onset of necking. We postulate this to be caused by the ease of forming complex defect structures for thicker NWs, which creates new dislocation sources other than the dislocation nucleation at the surface considered here. Our results provide an example where atomistic simulations and experiments complement each other to discover fundamental mechanisms of material deformation at the nanoscale.

4. Experimental Section

4.1. Penta-Twinned Ag NW Preparation

Ag NWs were synthesized by a modified polyol method.[26,27] In a typical synthesis, a solution of 55,000 MW polyvinylpyrrolidone (PVP) in ethylene glycol (5 mL, 40 mg/mL) was refluxed at 170 °C in a hot oil bath with constant stirring rate. NaCl in ethylene glycol (150 μL, 2.87 mg/mL) was added to the solution, followed by $AgNO_3$ in ethylene glycol (50 μL, 25 mg/mL). The solution was heated at the same temperature for about 15 min. The solution then turned yellow, showing the formation of Ag seed particles. $AgNO_3$ in ethylene glycol (1 mL, 25 mg/mL) was then added and reacted for 12 more minutes, resulting in a gray dispersion containing nanowires as well as low-aspect-ratio nanorods and particles. It should be noted that a thin PVP layer of a few nm's remains on the NWs. The resulting Ag nanowire product could be purified by cross-flow purification to remove excessive PVP, low-aspect-ratio nanorods and particles.[45]

4.2. Sources of Error in Stress Measurement

Because our MEMS device measures the force applied to the NW, measurement of stress requires an accurate estimate of the NW cross-sectional area. The cross-sectional area was calculated by considering a circular cross-sectional geometry with an area given by $\pi/4*D^2$ ($\sim 0.785*D^2$), where D is the diameter of the Ag NWs as measured from TEM images. SEM images of the cross-sectional geometry of the Ag NWs revealed that NWs with smaller diameters (<50 nm) have a circular geometry whereas NWs with larger diameters (>50 nm) transition to more well defined surface facets of a pentagonal geometry. The observation of smaller diameter NWs with circular cross-sections is consistent with previous work, which has shown that the higher temperature used here for synthesis (170 ºC) favors growth of circular NWs.[46] The observed transition to pentagonal geometries for thicker NWs is consistent with the NW growth mechanism, which is controlled by the concentration of the surface capping agent PVP.[26,27] Thicker NWs result from the growth of nanocrystals covered with a lower concentration of PVP which leads to a higher surface energy difference between the (100) and (111) facets as compared to thinner NWs with greater PVP surface passivation. This higher surface energy difference results in the relatively more aggressive growth of lateral (100) facets leading to thicker NWs with a more pentagonal geometry. In contrast to brittle semiconducting NWs (which have more well defined facets),[47] direct detailed characterization of the cross-sectional geometry of each NW tested is difficult therefore the stress for all NWs tested was calculated considering a circular geometry for consistency. It should be noted that this analysis may lead to a systematic error which underestimates the stress of the thicker Ag NWs by up to ~19%. We have performed atomistic simulations of penta-twinned Ag NWs with round cross sections, in which SFD formation are also observed. We do not observe any systematic difference between the round and pentagonal cross sections that can explain the size dependence of the yield behavior. An additional source of error in the stress comes from a layer of PVP and EBID carbon that is present on the NWs as a result of the synthesis and in-situ SEM/TEM manipulation and may also carry load in the tensile experiment if the layer is fully continuous along the NW length. A detailed analysis of this source of error is provided in the SI.

4.3. Predicting Yield Strain from Nucleation Theory

The energy barrier function $E_b(\varepsilon)$, shown in Figure 7, allows us to predict the critical elastic strain to nucleate a dislocation from the NW surface at the experimental strain rate. We will identify this critical strain for dislocation nucleation as the yield strain ε_y of the NW. From the classical nucleation theory,[48,49] the rate of dislocation nucleation under constant applied strain is,

$$I = N_s\ \nu_0\ \exp\left[-\frac{F_b\,(\varepsilon,\ T)}{k_B T}\right] \tag{1}$$

where N_s is the number of nucleation site, ν_0 is the characteristic attempt frequency, k_B is Boltzmann's constant, and T is the absolute temperature. $F_b\ (\varepsilon,\ T)$ is the activation Helmholtz free energy of dislocation nucleation at given strain ε and temperature T.

Assuming that the strain ε is increasing at a constant rate $\dot{\varepsilon}$, then the critical strain for dislocation nucleation (i.e. the yield strain ε_y) can be found by solving the following equation.

$$\frac{F_b\left(\varepsilon_y, T\right)}{k_B T} = \ln \frac{N_s\ \upsilon_0\ k_B\ T}{\dot{\varepsilon}\cdot\left(-\partial F_b/\partial\varepsilon\right)_{\varepsilon=\varepsilon_y}} \tag{2}$$

This equation is analogous to Equation (2) of Ref. [50] except that here we do not require the assumption that the elastic stress-strain relationship is linear.

The activation Helmholtz free energy can be approximated by,[49,51]

$$F_b\,(\varepsilon,\ T) = E_b(\varepsilon)\frac{\mu\,(T)}{\mu\,(0)} \tag{3}$$

where $\mu(T)$ is the shear modulus at temperature T and $\mu(0)$ is the shear modulus at zero temperature. From Figure 2 of Ref [52] it can be estimated that $\mu(T)/\ \mu(0)$ is about 0.90 for $T = 300$ K.

The number of nucleation sites N_s is estimated to be $5\ (L/\delta l)$, where L is the NW length, δl is the magnitude of repeat vector ½ <110> a_0 along the NW axis. The factor of 5 is to account for the five grains around the NW axis. The lattice constant of Ag is $a_0 = 4.09$ Å.

The attempt frequency factor ν_0 is chosen to fit the yield strain observed in MD simulations, for which the NW length is $L = 2.9$ D and the strain rate is $\dot{\varepsilon} = 10^7\ s^{-1}$. It is found that $\nu_0 = 10^{13}\ s^{-1}$ gives a good fit. The yield strain predicted by the nucleation theory for D = 6, 9, 12 nm is 6.27%, 5.95%, 5.80%, respectively. This matches well with direct MD simulations, which give 6.41%, 5.96%, 5.80%, respectively.

NANO MICRO small

To predict the yield strain at experimental condition, we use $L = 2\ \mu$m and $\dot{\varepsilon} = 5 \times 10^{-4}\ s^{-1}$. The predicted yield strain (corresponding to the first dislocation nucleation event) for D = 6, 9, 12 nm is 4.50%, 4.21%, 4.12%, respectively.

Supporting Information

Supporting Information is available from the Wiley Online Library or from the author. Section S1 describes an error analysis in the stress measurements. Section S2 summarizes details of the experimental in-situ TEM tensile tests. Section S3 shows details of necking in thick penta-twinned Ag NWs. Section S4 shows details of the steps of forming the stacking fault decahedron. Section S5 shows details of the change in dislocation nucleation mechanism in the low strain range.

Acknowledgements

T.F. and S.R. made equal contributions to this work. H.D.E. gratefully acknowledges support from NSF through award No. DMR-0907196. W.C. acknowledges support from NSF Grant CMS-0547681, and the Army High Performance Computing Research Center at Stanford University. J.H. acknowledges support from Northwestern University Materials Research Science & Engineering Center (NU-MRSEC, NSF DMR-0520513). K.K. acknowledges partial support from the Leading Foreign Research Institute Recruitment Program through the National Research Foundation of Korea funded by the Ministry of Education, Science and Technology (2011–0030065). The authors would like to thank W. Nix for insightful comments and discussions. The authors would also like to thank I. Petrov and E. Olson for their contribution in the development of the in-situ TEM holder.

[1] R. Agrawal, H. D. Espinosa, *J. Engin. Mater. Technol.* **2009**, *131*, 041208
[2] H. D. Espinosa, S. Berbenni, M. Panico, K. W. Schwarz, *PNAS* **2005**, *102*, 16933-16938
[3] H. Tang, K. W. Schwarz, H. D. Espinosa, *Phys. Rev. Lett.* **2008**, *100*, 185503
[4] Z. W. Shan, R. K. Mishra, S. A. S. Asif, O. L. Warren, A. M. Minor, *Nat. Mater.* **2008**, *7*, 115.
[5] J. R. Greer, W. C. Oliver, W. D. Nix, *Acta Mater.* **2005**, *53*, 1821.
[6] M. Dietiker, S. Buzzi, G. Pigozzi, J. F. Loffler, R. Spolenak, *Acta Mater.* **2011**, *59*, 2180.
[7] J. R. Greer, J. T. M. De Hosson, *Prog. Mater. Sci.* **2011**, *56*, 654.
[8] C. R. Weinberger, W. Cai, *J. Mater. Chem.* **2012**, *22*, 3277
[9] A. M. Leach, M. McDowell, K. Gall, *Adv. Funct. Mater.* **2007**, *17*, 43.
[10] C. Deng, F. Sansoz, *Nano Lett.* **2009**, *9*, 1517.
[11] H. Zheng, A. Cao, C. R. Weinberger, J. Y. Huang, K. Du, J. Wang, Y. Ma, Y. Xia, S. X. Mao, *Nat. Commun.* **2010**, *1*, 144
[12] H. S. Park, K. Gall, J. A. Zimmerman, *J. Mech. Phys. Solids* **2006**, *54*, 1862.
[13] S. S. Brenner, *J. Appl. Phys.* **1956**, *27*, 1484.
[14] G. Richter, K. Hillerich, D. S. Gianola, R. Monig, O. Kraft, C. A. Volkert, *Nano Lett.* **2009**, *9*, 3048.
[15] B. Kim, J. H. Seo, Y. Yoo, N. Y. Park, S. W. Yoon, H. Lee, S. Han, S. W. Lee, T. Y. Seong, S. C. Lee, K. B. Lee, P. R. Cha, H. S. Park, J. P. Ahn, *Nano Lett.* **2011**, *11*, 3499.
[16] B. Wu, A. Heidelberg, J. J. Boland, J. E. Sader, X. M. Sun, Y. D. Li, *Nano Lett.* **2006**, *6*, 468.
[17] Y. G. Sun, B. Mayers, T. Herricks, Y. N. Xia, *Nano Lett.* **2003**, *3*, 955.
[18] K. Lu, L. Lu, S. Suresh, *Science* **2009**, *324*, 349.
[19] D. C. Jang, C. Cai, J. R. Greer, *Nano Lett.* **2011**, *11*, 1743.
[20] L. Lu, Y. F. Shen, X. H. Chen, L. H. Qian, K. Lu, *Science* **2004**, *304*, 422.
[21] M. Dao, L. Lu, Y. F. Shen, S. Suresh, *Acta Mater.* **2006**, *54*, 5421.
[22] H. Idrissi, B. J. Wang, M. S. Colla, J. P. Raskin, D. Schryvers, T. Pardoen, *Adv. Mater.* **2011**, *23*, 2119.
[23] D. Bufford, H. Wang, X. Zhang, *Acta Mater.* **2011**, *59*, 93.
[24] X. Y. Li, Y. J. Wei, L. Lu, K. Lu, H. J. Gao, *Nature* **2010**, *464*, 877.
[25] M. Lucas, A. M. Leach, M. T. McDowell, S. E. Hunyadi, K. Gall, C. J. Murphy, E. Riedo, *Phys. Rev. B* **2008**, 77, 245420
[26] Y. G. Sun, B. Gates, B. Mayers, Y. N. Xia, *Nano Lett.* **2002**, *2*, 165.
[27] Y. G. Sun, Y. D. Yin, B. T. Mayers, T. Herricks, Y. N. Xia, *Chem. Mater.* **2002**, *14*, 4736.
[28] C. J. Johnson, E. Dujardin, S. A. Davis, C. J. Murphy, S. Mann, *J. Mater. Chem.* **2002**, *12*, 1765.
[29] Y. Zhu, H. D. Espinosa, *Proc. Natl. Acad. Sci. USA* **2005**, *102*, 14503.
[30] T. Filleter, R. Bernal, S. Li, H. D. Espinosa, *Adv. Mater.* **2011**, *23*, 2855.
[31] R. Agrawal, B. Peng, E. E. Gdoutos, H. D. Espinosa, *Nano Lett.* **2008**, *8*, 3668.
[32] B. Wu, A. Heidelberg, J. J. Boland, *Nat. Mater.* **2005**, *4*, 525.
[33] G. Y. Jing, H. L. Duan, X. M. Sun, Z. S. Zhang, J. Xu, Y. D. Li, J. X. Wang, D. P. Yu, *Phys. Rev. B* **2006**, 73.
[34] M. T. McDowell, A. M. Leach, K. Gall, *Nano Lett.* **2008**, *8*, 3613.
[35] T. Zhu, J. Li, A. Samanta, A. Leach, K. Gall, *Phys. Rev. Lett.* **2008**, *100*, 1.
[36] M. J. K. H. W. Sheng, A. Cadien, T. Fujita, M. W. Chen, *Phys. Rev. B* **2011**, *83*, 134118.
[37] A. F. Voter, Los Alamos unclassified technical report # LA-UR 93–3901 **1993**, http://library.lanl.gov/cgi-bin/getfile?LA-UR-93-3901.pdf
[38] M. I. B. S. M. Foiles, M. S. Daw, *Phys. Rev. B* **1986**, *33*, 7983.
[39] MD++ simulation package. http://microstanfordedu/MDpp/
[40] S. Plimpton, *J. Chem. Phys.* **1995**, *117*, 1.
[41] J. A. Zimmerman, E. B. Webb, J. J. Hoyt, R. E. Jones, P. A. Klein, D. J. Bammann, Modelling, *Sim. Mater. Sci. Engin.* **2004**, *12*, S319.
[42] A. M. Pendas, *J. Chem. Phys.* **2002**, *117*, 965.
[43] H. S. Park, W. Cai, H. D. Espinosa, H. Huang, *MRS Bull.* **2009**, *34*, 178.
[44] S. Ryu, K. Kang, W. Cai, *Proc. Natl. Acad. Sci. USA* **2011**, *108*, 5174.
[45] K. C. Pradel, K. Sohn, J. X. Huang, *Angew. Chem. Int. Ed.* **2011**, *50*, 3412.
[46] X. M. Sun, Y. D. Li, *Adv. Mater.* **2005**, *17*, 2626.
[47] R. A. Bernal, R. Agrawal, B. Peng, K. A. Bertness, N. A. Sanford, A. V. Davydov, H. D. Espinosa, *Nano Lett.* **2011**, *11*, 548.
[48] R. Becker, W. Döring, *Ann. Phys.* **1935**, *24*, 719.
[49] S. Ryu, K. Kang, W. Cai, *Proc. Natl. Acad. Sci. USA* **2011**, *108*, 5174.
[50] T. Zhu, J. Li, A. Samanta, A. Leach, K. Gall, *Phys. Rev. Lett.* **2008**, *100*, 025502
[51] S. Ryu, K. Kang, W. Cai, *J. Mater. Res.* **2011**, *26*, 2335.
[52] J. R. Neighbours, G. A. Alers, *Phys. Rev.* **1958**, *111*, 707.

Received: March 8, 2012
Published online: July 25, 2012

